Design, Analysis of a Seven-Phase fault-tolerant Bi-Harmonic Permanent Magnet Machine with Three Active Air Gaps for In-Wheel Traction Applications

J. Gong, X. Wang, B. Zhao, F. Tan, E. Semail, N. K. Nguyen, N. Bracikowski

***Abstract*—For the requirements of in-wheel traction systems, a new motor is proposed based on a specific property of multiphase machines: the ability in vector control to develop smooth torque at low speeds by using simultaneously the first and third harmonics to generate p and 3p polarities. From an initial fault-tolerant seven-phase axial–flux machine with two outer axial rotors for small vehicles such as moto/scooter is born the proposed motor just by adding magnets in the cylinder closing the two 2p-pole axial rotors of initial in-wheel motor, this addition creates thus a third radial rotor with 3p poles without changing the global volume. With an increase by 51% of the torque density, this more expensive motor can be considered in comparison with the initial in-wheel motor as a modular solution. With the same volume, more constraining torque requirements for higher acceleration and slopes can be obtained. The possibility to use different polarities with quite non-sinusoidal emf but without increase of the torque ripples e is verified in 3D-FEM simulation and in a manufactured 28 slots prototype with 12/36 poles. Experimental results are given to prove the effectiveness of the proposal.**

***Index Terms*—double polarity, seven-phase machine, in-wheel, permanent magnet synchronous machine**

NOMENCLATURE

FSCW	Fractional slot concentrated winding
ISDW	Integrated slot distributed winding
AFPM	Axial flux permanent magnet machine
HFPM	Hybrid (axial-radial) flux permanent magnet Machine
TORUS-S	Double-sided axial flux with output rotors and internal slotted stator
SPM	Surface-mounted permanent magnet machine
IPM	Interior permanent magnet machine
FOC	Field-oriented control

This paper is properly extended and modified in accordance with IEEE PES policy from Post-conference papers of ICEM 2022, which is "Seven-phase axial and radial flux in-wheel machine with three active air gaps", by Jinlin Gong, Benteng Zhao, Eric Semail, Ngac-Ky Nguyen and Nicolas Bracikowski.

Jinlin Gong, XiuLin Wang and Fei Tan are with the School of Electrical Engineering of Shandong University, Jinan, China (email: gongjinlin@sdu.edu.cn). Benteng Zhao is with China Astronaut Research and Training Center, Beijing, China (email: zbenteng@foxmail.com). Eric Semail is with the Engineering School of Arts et Métiers ParisTech, Lille, France (email: eric.semail@ensam.eu). Ngac Ky Nguyen is with Arts et Métiers ParisTech, Lille, France (email: NgacKy.NGUYEN@ensam.eu). Nicloas Bracikowski is with IREENA Laboratory of Nantes University, Saint-Nazaire, France (email: nicolas.bracikowski@univ-nantes.fr).

I. INTRODUCTION

Electric vehicles (EVs), which are quieter, less air polluting and thus more environmentally friendly than traditional internal combustion engine vehicles, are becoming more and more popular. As one of the key components of EV traction system, the in-wheel electrical machine basically integrates the power, transmission and braking devices into the wheel hub, thus greatly simplifies the structure of electric vehicles, which makes its application more and more widespread [1].

Permanent magnet machine with outer rotor structure is one of the most common in-wheel electrical machine, due to the high torque density and simple mechanical structure [2]. According to the flux directions, the in-wheel machines with outer rotor structure can be mainly classified into two groups, i.e. radial and axial flux machines [3].

Among the radial flux machines with outer rotor, the surface-mounted permanent magnet machines (SPM) are the most classical and popular for the commercialization. An SPM with bar-wound conductors for a tooth-wound configuration in stator is studied in [4]. The bar-wound conductor can achieve better heat transfer between copper and stator iron than the multi-stranded windings, so as to improve the short duty torque capability. In [5], V-shaped magnet embedded in the external rotor is designed and the enhanced flux concentration is achieved, thus high torque and power density can be obtained for low-speed electric bicycle applications. Twelve different radial flux PM machines are compared in [6]. Machines with interior PM rotors have 9%-14% less developed torque-per-copper-loss performance than machines with surface-mounted PM rotors. On contrary, these machines have a much better constant power speed range.

Flux modulation machines are characterized by high torque density and widely studied in literature recent years. In [7], an interesting axial-radial but with one internal rotor is proposed. Windings achievement is not clearly shown in the virtual prototype. In [8] an outside rotor flux switching PM machine (OR-FSPM) with wedge-shaped magnets has been optimally designed. With flux switching machine, losses in the stator PM magnets must be managed. In [9] a novel OR-FSPM with segmented PM is proposed and its higher suitability for in-wheel light traction application is demonstrated. Vernier

V-type and spoke-type PM machines are investigated respectively in [10] [11] and proven to be interesting for in-wheel application even if PM losses are still sensitive.

Due to the advantages of fault-tolerant operation and capability of operating at high temperature, switched reluctance machine (SRM) can also be a viable candidate for in-wheel traction application. A new SRM structure of 12/26 pole segmented rotor with centralized winding arrangement is proposed, which has high specific torque and can replace BLDC motor while providing low-cost solution [12]. However, the torque fluctuations at low speed and the acoustic noise restrict always its applications. In order to overcome this, an external-rotor SRM with 6 stator poles and 10 rotor poles is designed which improved torque ripple [13]. A new modular spoke PM motor was proposed in [14], which can facilitate the manufacture. Halbach array structure with the original spoke-type PM can also improve the torque density and flux weakening capability [15] [16], however, its specific PM magnetization can slow down the fabrication and the cost of high.

Compared to radial flux machine, under the constraint of the same volume, the same speed and the flux density in the air gap, the axial flux machine (AFM) has a good torque density in terms of volume and mass [3]. Moreover, AFM are particularly studied for in-wheel applications due to the compact structure characteristic, especially with the limitation of axial length. Nevertheless, axial forces induce mechanical constraints unless symmetrical structure is adopted. Then, axial flux used for direct drive is usually a sandwich structure with a stator sandwiched between two rotors, or a rotor between two stators [17] [18]. In [19], a double-stator single-rotor axial flux motor embedded with NdFeB magnet was optimized and installed directly inside the wheel, providing a promising solution for direct drive electric vehicles. By eliminating the back iron of the stator, YASA motor can further improve the torque density in terms of mass [20] [21]. The reduction of the torque ripple of YASA motor is studied by optimizing the skew angle of the rotor magnet, with the increase of the skew angle, the torque ripple decreases quickly, but the efficiency is slightly reduced [22]. Furtherly, for the coreless AFM, the windings can be fixed by plastic composite material which not only improve the torque density and also reduce the cogging torque [23] [24]. However, the resulting larger magnetic air gap and the heat dissipation of the windings limit its applications. Yokeless stator AFPMs having fractional slot concentrated winding (FSCW) and integrated slot distributed winding (ISDW) are comparative studied for electrical vehicle traction applications [25]. The comparative results shows that the ISDW-AFPM machines with IPM structure exhibit better both the torque/power capacity and the flux weakening capacity. However, FSCW-AFPM machines are characterized by the highest torque/power density due to the compact structure.

Four types of motors are compared in [26]，including one 3-phase IPM machine with V-shape PMs [5], one 5-phase SPM machine [27], one 7-phase AFM of sandwich structure [28] and finally one hybrid flux (radial and axial) machine with a third rotor with V-shape PMs added to the AFM. The results show that the multi-phase AFM have higher torque density and higher fault tolerance, and are very suitable for direct drive applications.

In this paper, the practical objective is to find a modular solution for in-wheel outer rotor machine for small vehicles such as moto, scooter, etc. The modularity must be understood as the possibility to propose in a same external volume two motors with different torque densities. It can be imagined that the motor with the highest torque density is more adapted for a traction motor with higher requirements for slope, acceleration capacity or mass of load. The initial proposed machine with two axial rotors is a seven-phase slotted TORUS-S. Three-phase machine TORUS-S presents torque ripples (Fig. 11 of [29]) unless pie-shaped winding and with skewed magnets. With a seven phase the torque ripples are lower [30] with lower constraints for the designer [31], because the interaction between harmonics of electromotive force and currents are different than for a three-phase machine (paragraph IV of [29]). Moreover, fault tolerance to open-phase is also obtained with a seven-phase machine. Based on an initial structure of 7-phase AFM with one stator sandwiched between two rotors, a third rotor with PM radial magnetized is added to make active the end-windings. Thanks to the addition of the third rotor, a closed machine is naturally constructed with no need of mechanical cover between the two rotors as with the initial 7-phase AFM. Therefore, the torque density can be furtherly improved if the global volume is kept. A solution with a third rotor is already discussed in chapter 2 in [17], but the polarity (p pairs of pole) of the third rotor is the same than this one of the two other axial rotors. In our case the stator is also toroidal type but on contrary it is magnetic with slots inside SMC core. In this paper, the specific property of 7-phase machine is employed, i.e. the possibility to use third harmonic component without increasing torque ripples [30]. With 3p pair poles the third rotor is thus more compact. Moreover, the operational speed range can be enlarged, due to the harmonic decoupling principle of multiphase machine [31].

The paper is organized as follows. In Section II, the machine geometry topology is introduced, and the main preliminary dimensions are initially calculated. In Section III, the toroidal winding of the stator is designed by using winding shifting method, and the considerations for the selection of the slot and the rotor poles are given. In section IV, a 7-phase hybrid flux PM machine (HFPM) of three rotors with 28 slots 12/36 poles is preliminarily designed, the electromagnetic performance such as back electromotive force (EMF), cogging torque, and output torque are studied using finite element method (FEM). In section V, experimental results are performed on a prototype in order to validate the ones of FEM. And finally, some remarks on the novel machine are given in the conclusion of section VI.

II. Structure Consideration

A. Geometrical topology of hybrid flux PM machine (HFPM)

Among various existing structures of AFPM, the NN-type TORUS AFPM with toroidal winding [29][32] is selected here as initial machine. It possesses one torus-shape stator

sandwiched between two external rotors as shown in Fig. 1(a) with inactive end-windings on axial direction. The addition of a 3rd rotor with PMs radially magnetized can make active these end-winding which is shown in Fig. 1(b). The output torque density can thus be improved. The PMs of the two axial rotors are surface mounted which is easier for fabrication and saves the axial length. The PMs of the radial rotor are V-shaped and embedded on it, which can reinforce the flux density in the air gap due to the flux focusing effect. The three outer rotors are connected together mechanically and contribute to the output torque. Fig. 1(c) shows the exploded view of the whole machine. A closed form machine is thus defined by the three external rotors which can be inserted in the wheel. No more additional covers are needed compared to traditional machines.

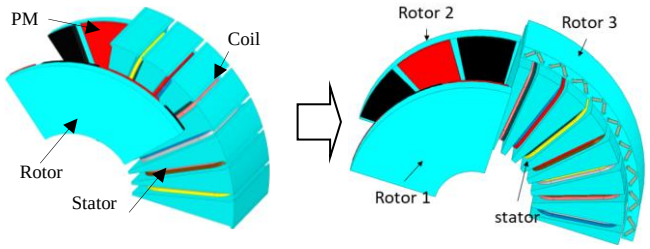

(a) one-fourth of the initial AFPM without mechanical connection between the two rotors

(b) one-fourth of the new HFPM structure

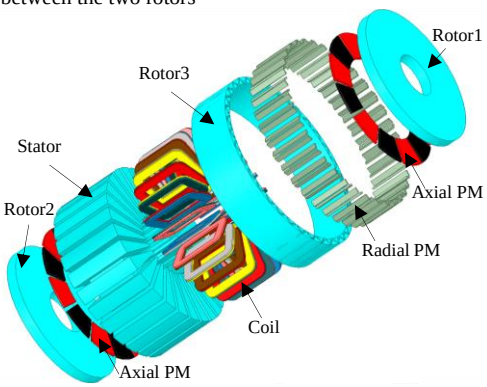

(c) the exploded view

Fig. 1. TORUS HFPM with two axial and one radial rotors

For the requirement of the in-wheel traction system, i.e. high torque at low speed and large constant power region, 7-phase bi-harmonic machine is preferred. The injection of high order harmonic of current improves the output torque density while keeping the same level of torque ripple compared to a 3-phase sinusoidal machine [33]. Moreover, the wide speed range can also be obtained due to the specificity of the multiphase bi-harmonic machine [31]. The number of poles of the 3rd rotor is designed to be three times of the two axial rotors, and the operational speed range can be enlarged through the electronic pole changing effect.

B. *Machine design procedure*

The flowchart of the design process is shown in Fig. 2. Firstly, the phase number is selected. The choice of the number of phases is linked with three simple constraints[31]:

Cr1. the ability to work in fault mode without too much torque ripple,

Cr2. the ability to use the third harmonic to increase the torque density of the machine,

Cr3. a minimum number of legs for the VSI which is supposed to supply the machine.

These three constraints eliminate the 5-phase machine for which it is difficult to verify simultaneously the constraints Cr1 and Cr2. Therefore, the seven-phase machine is chosen. Then the fractional slot concentrated Wingding (FSCW) is designed by using winding shift technique. Secondly, for the required performances, the preliminary dimensions are determined. Thirdly, the dimension parameters of the third rotor are optimized. Fourthly, finite element method is used to validate and adjust the preliminary design. Finally, a prototype is made and experiment tests are done in order to validate the design.

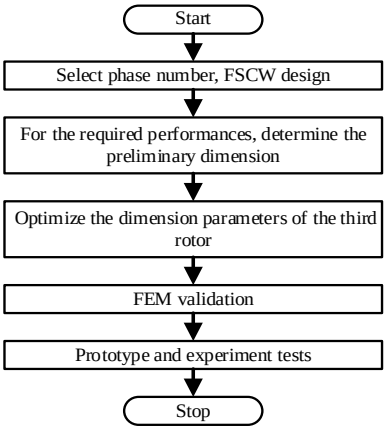

Fig. 2. Flow chart of design algorithm

C. *Preliminary sizing equations*

C.1 Torque expression

Ignoring magnetic saturation and reluctance effects, 7-phase machines can be considered as three fictitious two-phase machines and one single-phase machine with magnetic decoupling [34]. Each fictitious machine is characterized by a set of harmonics shown in Table I. The fictitious machines are magnetically independent, but mechanically and electrically connected, i.e. the total output torque is the sum of the fictitious machines. It should be noted that zero-sequence machine is not considered when the windings of the machine stator are star-connected.

TABLE I THE HARMONICS CORRESPONDING TO FICTITIOUS MACHINES

Fictitious machines	Associated odd harmonics
Primary machine called M1	1,13,15,27 …7*k±1
Secondary machine called M5	5,9,19,23 …7*k±2
Third machine called M3	3,11,17,25 …7*k±3
Zero-sequence machine	7, 21, …, 7*k

Using fictitious machines approach [30], the electromagnetic torque of the seven-phase machine is derived with the formula (1).

$$T_{em} = \frac{\overrightarrow{e_{M1}}\overrightarrow{i_{M1}} + \overrightarrow{e_{M3}}\overrightarrow{i_{M3}} + \overrightarrow{e_{M5}}\overrightarrow{i_{M5}}}{\Omega} \quad (1)$$

where Ω is the rotating speed of the rotor in rad/s; $\overrightarrow{e_{Mk}}$ and $\overrightarrow{i_{Mk}}$ are the back-emf and the current vectors of fictitious machine M_k with k=1, 3, 5. They are obtained by vector projection of back-emf and current vectors in the associated eigenspace of each fictitious machine, defined by the classical Concordia transformation.

In each fictitious machine, because of the main harmonic current injection, it can be considered that only the main harmonic is contributing significantly to the torque. Thus, the expression of the back-emf in each fictitious machine can be approximated by:

$$\overrightarrow{e_{Mk}} = \sqrt{\frac{7}{2}} E_k \sqrt{2}\left(-\sin(kp\theta)\overrightarrow{x_{\alpha k}} + \cos(kp\theta)\overrightarrow{x_{\beta k}}\right) \tag{2}$$

where E_k the RMS value of the harmonic k of back-emf, k=1, 5, 3 for the fictitious machine M1, M5 and M3, respectively; p is the number of poles; θ is angle shown in Fig. 3(a); $\overrightarrow{x_{\alpha k}}$, $\overrightarrow{x_{\beta k}}$ are the orthonormal unit vector in α-β coordinate system.

As the adopted control strategy in the design step is classically maximum torque per ampere (MTPA), the current vector is co-linear with the back-emf vector. The current vector can thus be expressed:

$$\overrightarrow{i_{Mk}} = \sqrt{\frac{7}{2}} K_0 \, E_k \sqrt{2}\left(-\sin(kp\theta)\overrightarrow{x_{\alpha k}} + \cos(kp\theta)\overrightarrow{x_{\beta k}}\right) \tag{3}$$

where the value of K_0 is related to the linear current density chosen for the design of the machine.

Substitute (2) and (3) into (1), the output torque with three injected current harmonics can be obtained as follows:

$$T = 7K_0E_1^2\left(1+(E_3/E_1)^2+(E_5/E_1)^2\right)/\Omega \tag{4}$$

C.2 Flux formulation

Fig. 3 (a) shows the permanent magnet of one pole. The center of the pole is selected as the polar axis, and the axis of one winding is considered as the reference axis. In order to describe the air gap flux density distribution in the air gap, a point P in the air gap is selected, as shown in Fig. 3 (a). Respected to the polar axis and the reference axis of one winding, the mechanical angles of the point P are ζ_R and ζ_S.

Neglecting the slot effect, the flux leakage between PMs, the saturation of material and the coupling between the two rotors, the flux density in the air gap due to PMs is supposed to have roughly a rectangular distribution as shown in Fig. 3 (b), in which b_{E1} is the pole-arc coefficient, p is the pole-pair number.

The flux density in the air gap of the two axial direction can be expressed in (5).

$$B_{E1}(\zeta_R) = \sum_{i=0}^{\infty} \alpha_{iE1}\cos(ip\zeta_R) \tag{5}$$

Similarly, the flux density in the radial air gap due to the 3rd rotor of 3p pole pairs can be expressed in (6).

$$B_{E2}(\zeta_R) = \sum_{i=0}^{\infty} \alpha_{iE2}\cos(i3p\zeta_R) \tag{6}$$

Where α_{iE1} and α_{iE2} are the coefficients of Fourier series.

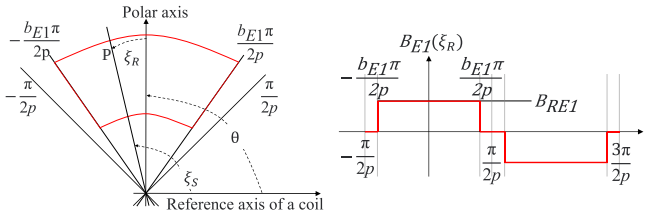

(a) (b)

Fig. 3. Air gap flux density representation of (a) a spatial point **P** in the air gap (b) wave form

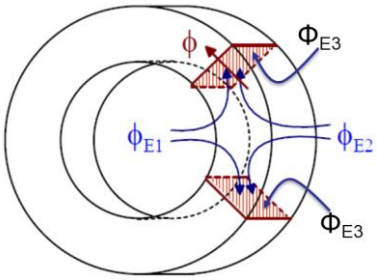

Fig. 4. Flux of two simple coils of the stator due to PMs

The flux of one coil of the stator due to PMs is shown in Fig. 4. It can be seen that the flux is composed by three parts, Φ_{E1}, Φ_{E2}, Φ_{E3}, i.e. two axial and one radial. The flux of one coil can then be expressed as follows:

$$\phi(\zeta_s,\theta) = k_p \frac{\phi_{E1}(\zeta_s,\theta)+\phi_{E2}(\zeta_s,\theta)+\phi_{E3}(\zeta_s,\theta)}{2} \tag{7}$$

Where k_p is pitch, Φ_{E1}, Φ_{E2}, Φ_{E3} are the air gap flux per pole due to the PMs of the three rotors, and Φ_{E1}=Φ_{E2}.

The air gap flux per pole can be expressed as follows:

$$\phi_{E1}(\zeta_s,\theta) = \int_{r=R_1}^{r=R_2}\int_{\zeta_s=-\frac{\pi}{2p}}^{\zeta_s=\frac{\pi}{2p}} B_{E1}\,dr\,d\zeta_s \tag{8}$$

$$\phi_{E3}(\zeta_s,\theta) = l\cdot R_3\int_{\zeta_s=-\frac{\pi}{2p}}^{\zeta_s=\frac{\pi}{2p}} B_{E3}\,d\zeta_s \tag{9}$$

Where R_1, R_2 are the inner and outer radius of the axial PMs, l is effective axial length of the machine, R_3 is inner radius of the third rotor.

The flux per phase can then be obtained,

$$\phi(\theta)_{\text{phase}} = k_w 2pN_s\phi(\theta) \tag{10}$$

Where k_w is the winding factor, N_s is the number of coils per slot per phase.

The back-emf can be obtained through the derive of the flux in (10), and expressed as follows,

$$e(t)=\frac{8k_{w1}N_s\omega B_{RE1}}{\pi}\left(R_2^2-R_1^2\right)\sum_{i=0}^{\infty}\frac{\sin\left(h\frac{\pi}{2}\right)}{h}\sin\left(h\frac{b_{E1}\pi}{2}\right)\sin\left(h\omega t\right) \quad (11)$$

$$+\frac{8k_{w3}N_s\omega B_{RE2}}{\pi}R_3 l\sum_{i=0}^{\infty}\frac{\sin\left(3h\frac{\pi}{2}\right)}{h}\sin\left(h\frac{b_{E3}\pi}{2}\right)\sin\left(3h\omega t\right)$$

Where k_{w1}, k_{w3} are the winding factors of the fundamental and the third harmonics, ω is the electrical angular frequency, B_{RE1} and B_{RE2} are the average flux density in the axial and radial air gap due to PMs, h=2i+1.

Substitute (11) into (4), the output torque can be calculated according to the design parameters, and therefore, the preliminary dimensions of the machine can be obtained.

III. WINDING DESIGN

A. *Fractional slot concentrated winding design*

Fractional slot concentrated winding (FSCW) is easy to manufacture, with high slot filling coefficient and thus high torque density. It is preferred by the machines with large number of poles. Its main challenge is the rich content of magnetomotive force (mmf) space harmonics, including both sub- or sup-order. These parasitic space harmonics can lead to eddy current loss, vibration, noise, local core saturation, and so on, thus reducing the performance of the machine. To avoid these drawbacks, it is necessary to choose the suitable slot/pole combination.

The choice of slot/pole number combination is the most important for FSCW design, which is directly related to the performance of the machine [35]. There are many criteria for the selection of the pole/slot number combination, two of them are considered in this paper. One is the winding coefficient of the working harmonic. The higher of the value is, the higher torque density can be obtained. For the 7-phase machine of this paper, the working current harmonics are the fundamental and 3rd harmonics. The 5th harmonic is often not taken into account, because of the small value of back-emf, i.e., less important to the output torque. The second criterion is that the parasitic harmonic content of the mmf should be low, in order to reduce machine losses both in iron and PMs when the fundamental and 3rd current harmonics are injected simultaneously.

Using the winding function theory [36], the winding factor corresponding to the v^{th} harmonic of the mmf can be calculated as follows,

$$k_v=\frac{m}{Q_0}\left|\sum_{i=1}^{Q_0}d_{i,c}e^{-j\frac{2\pi}{Q_0}ip_0v}\right|,\quad \forall v,c\in N \qquad (12)$$

where, Q_0 is the number of stator slots of the unit machine, p_0 is the number of rotor poles of the unit machine, j is the imaginary number unit, $d_{i,c}$ is the elements of row i and column c in the winding distribution matrix. The winding factors of 7-phase machines, i.e. k_1, k_3 and k_5, are shown in Table II.

TABLE II. WINDING FACTORS OF 7-PHASE MACHINES FOR THE FIRST, THIRD AND FIFTH HARMONICS

Q\2*p*	2	4	6	8	10	12	14	16	18
	0.43	0.78	0.97	0.97	0.78	0.43		0.43	0.78
7	0.97	0.43	0.78	0.78	0.43	0.97	-	0.97	0.43
	0.78	0.97	0.43	0.43	0.97	0.78		0.78	0.97
	1.00	0.43	0.78	0.78	0.90	0.97		0.97	0.90
14	1.00	0.97	0.43	0.43	0.22	0.78	-	0.78	0.22
	1.00	0.78	0.97	0.97	0.62	0.43		0.43	0.62
		0.29	0.43	0.56	0.68	0.78		0.92	0.97
21		0.73	0.97	0.91	0.73	0.43	-	0.41	0.78
		0.82	0.78	0.12	0.46	0.97		0.24	0.43
	0.99	1.00	0.33	0.43	0.53	0.62		0.78	0.84
28	0.94	1.00	0.80	0.97	0.94	0.90	-	0.43	0.11
	0.85	1.00	0.84	0.78	0.28	0.22		0.97	0.80
			0.24	0.35	0.43	0.49		0.65	0.70
35			0.24	0.76	0.97	0.68	-	0.78	0.48
			0.51	0.63	0.78	0.13		0.35	0.28

For the first criterion, the winding factors of slot/pole number combination of 7 phases, 14 slots /12 poles can be selected. The winding factors of the fundamental and 3rd harmonic are 0.97 and 0.78 respectively. The mmf spectrum is analyzed, as shown in Fig. 5. It can be seen that the working harmonic is the 6th with the fundamental current supplied in Fig. 5(a), and the 18th with the 3rd harmonic current supplied in Fig. 5(b). Unfortunately, the parasitic harmonics of mmf are abundant, especially those with large amplitudes, such as the 8th, the 20th in Fig. 5(a), and the 4th in Fig. 5(b). In order to reduce the parasitic harmonics, the stator shift technique is adopted [37]. The number of poles is kept to be constant, and the number of slots is doubled, i.e., from 14 to 28. The second 14 slots are shifted by an electrical shift angle from the first 14 slots. The final amplitude of k^{th} MMF harmonic of the novel winding topology is expressed in (13) .

$$v_{\alpha k}=v_{dk}\cos\left(\frac{k\alpha}{2}\right) \qquad (13)$$

$$\alpha=j\times 360^{o}/Q,\quad j=1,2,3... \qquad (14)$$

Where v_{dk} is the amplitude of the k^{th} MMF harmonic of the 14 slots /12 poles winding; α is the mechanical shift angle which is a discrete number and Q is the number of stator slots. A new winding topology of 28 slots /12 poles is realized. It can be noted that in Fig. 5, the mmf spectrums under both the fundamental and the 3rd harmonic current injection are improved, in which the loss-producing harmonics are greatly reduced. At the same time, the winding factors are also of the same high values, K_1=0.97, K_3=0.78. As a result, higher torque densities and less losses can be achieved.

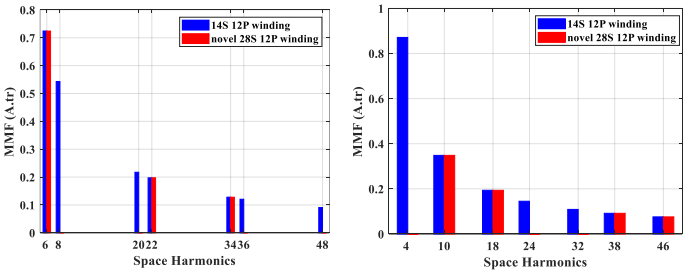

(a) (b)

Fig. 5. mmf harmonic spectrum with injection of (a) fundamental current (b) 3rd harmonic of current

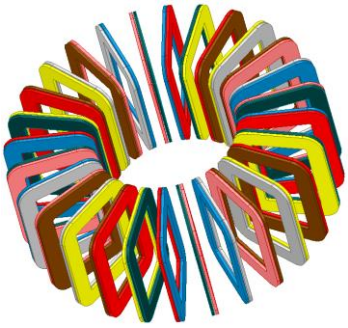

Fig. 6. Novel 28-slot/12-pole toroidal winding topology

B. Realization using Toroidal

The new winding topology is shown in Fig. 6. The coils of the same phase are represented by the same color, and there are seven colors in total. It can be seen that the proposed winding is a double layer one, i.e. 2 coils of different colors in each slot. Taking two coils in red color as an example. The two adjacent coils are of the same phase and separated by one slot. The realization of the two coils can be shown in Fig. 7. The two coils are wound separately in two different slots with a reverse direction, and the ends are connected at the inner radius of the stator. Because it is a ring winding, and the non-overlapping characteristics can be kept, even with the application of stator shift technique.

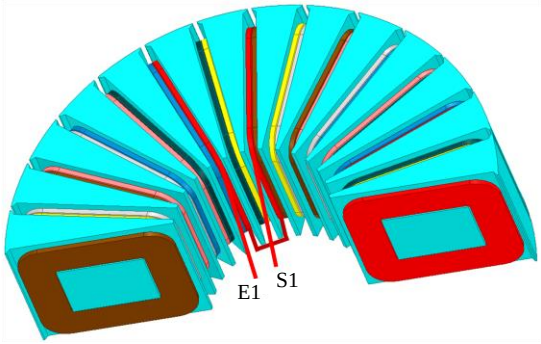

Fig. 7. The connection way of the novel toroidal +winding topology

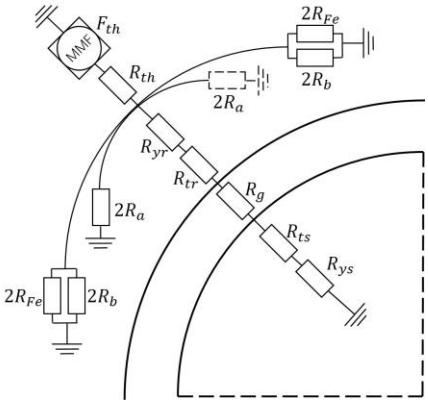

Fig. 8. Equivalent magnetic circuit based on Thevenin theorem

C. V-shaped PM radial rotor design

V-shaped PMs are adopted by the radial rotor which can enhance the flux density in the air gap and improve the flux weakening ability. An equivalent magnetic circuit using Thevenin's theorem [38] is built for the modeling and the design of the radial rotor to obtain the desired radial air gap flux density and minimum machine radial radius and PM volume, as shown in Fig. 8. The optimization objective is to find the minimum machine radius and PM volume under air-gap flux density, pole-arc coefficient and geometric limits using *gamultiobj* function.

In Fig. 8, R_{tr}, R_{ts}, R_{ys}, R_{yr} are related to the reluctance of stator and rotor teeth and yokes; R_g is the reluctance of the air gap; R_b is the reluctance of flux barriers; R_{Fe} is the reluctance of the saturated iron bridges under one pole. Using Thevenin-equivalent theory, the following relationship can be obtained:

$$F_{th} = F_m - R_{th}\Phi_{sat} \tag{15}$$

Where F_{th} is the equivalent Thevenin mmf; F_m is the mmf generated from PMs; R_{th} is equivalent Thevenin reluctance which can be obtained by the sum of PMs reluctance and internal airgap around the PMs; Φ_{sat} is the flux required to saturate the iron bridges which can be calculated as follows,

$$\Phi_{sat} = B_{sat} w_{Fe} k_f L \tag{16}$$

Where B_{sat} is the flux density in saturated iron and K_f is the stacking factor for the lamination; L is the axial length of the magnet; w_{Fe} is the sum of the iron bridge widths under one pole.

IV. Finite Element Verification for The Prototype

The 3D-FEM is used to validate the pre-design of the HFPM machine. Table III presents the main specifications of the 7-phase 28-slot 12-pole/36-pole machine.

TABLE III MAIN SPECIFICATIONS OF THE HFPM

Parameters	Value
Number of phases	7
Number of slots	28
Number of pairs of poles (axial rotors) p	6
Number of pairs of poles (radial rotors) 3p	18
Stator core outer diameter (mm)	145.9
Stator core inner diameter (mm)	50.6
Slot dimension (mm)	4.3*13.1
Number of coils per slot	22
Axial length of stator core (mm)	47.6
Axial length of axial rotor core (mm)	5.3
Thickness of axial magnet (mm)	1.9
Thickness of air gaps (mm)	1
Outer diameter of radial rotor (mm)	183.54
Inner diameter of radial rotor (mm)	161
Axial length of the radial rotor (mm)	47.6
Thickness of V-shape magnet (mm)	2
Rated speed (rpm)	600
Rated torque (Nm)	9.5
Rated phase current (ARMS)	3.15
DC Voltage (V)	96

A. Flux density distribution

Fig. 9 shows the 1/4 structure of the original double polarity fault tolerant machine with 7 phases, 28 slots, 12 poles/36 poles, and its flux density distribution under no-load condition. As can be seen, on the stator core and the two axial rotors, the maximum of magnetic flux density is about 1.6T. For the radial rotor, the iron bridge is saturated and the maximum value is 2T.

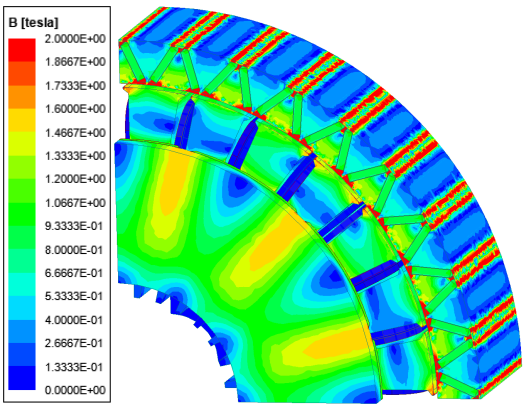

Fig. 9. 3D FEM predicted flux density distribution

B. *Air-gap flux density, flux linkage and Back-EMF*

Fig. 10 shows the FEM predicted air-gap flux density distribution with 1/4 machine structure. Fig. 10 (a) shows the air gap flux density with two axial PM rotors, and Fig. 10 (b) shows the one with radial PM rotor. The mean value of the two flux density are 0.81T and 0.82T, respectively. It can be noted that the number of poles of the radial rotor is 6p instead of 2p for the two axial rotors.

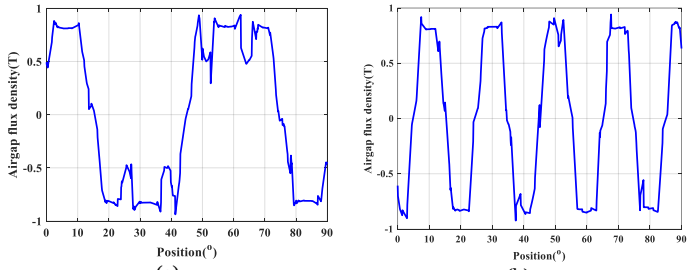

(a) (b)

Fig. 10. Air-gap flux density of HFPM machine at 600 rpm at (a) axial (b) radial direction

Fig. 11 shows the flux linkage and its harmonic spectrum of one phase in no-load condition. It can be noted that the 1st and the 3rd harmonic component are dominant and ratio of Φ_3/Φ_1 is equal to 0.41. In order to keep low torque ripples with easy control when one phase is opened, the 5th and the 9th harmonics of electromotive force are imposed to be small (see Fig. 12) and will be neglected [30].

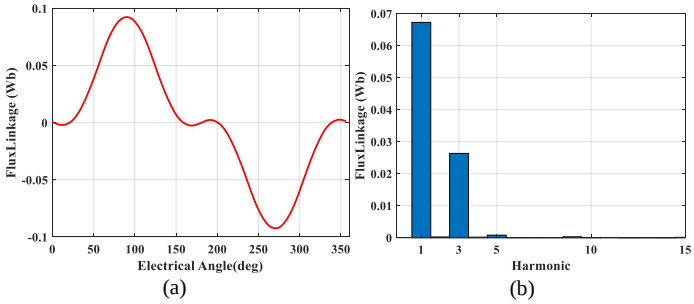

(a) (b)

Fig. 11. FE validation of HFPM machine at 600 rpm with (a)Flux linkage (b) harmonics

Fig. 12 shows the back-EMF and its harmonic spectrum of one phase at no-load. The 1st and the 3rd harmonics are of the same order of magnitude, which consists well with the specificity of the bi-harmonic machine.

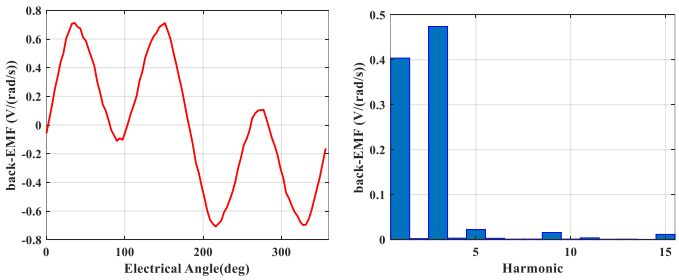

(a) (b)

Fig. 12. FE validation of HFPM machine at 600 rpm with (a) back-EMF (b) harmonics (E_1: 0.4V/rad/s; E_3: 0.48 V/rad/s: E_3/E_1=1.2)

C. *Electromagnetic Torque*

As it can be considered that the flux linkage contains only the first and third harmonic, only the first and third harmonics of current are therefore injected. For a given peak value of current, a comparison of the torques obtained with MTPA strategy as presented in II-C is made considering three kinds of supply: with only the first, only the third, and both the first and the third sinusoidal currents as shown in Fig. 13. It can be remarked that the peak value of the currents is imposed equal. The waveforms of the torque at 600 rpm speed are then shown in Fig. 14. The torque ripples can be considered as low even when two harmonics of close amplitudes are injected (about 6 %), and the fundamental main frequency of the torque ripple is 840Hz as expected (14*6*600/60). It confirms that the first and third harmonic interactions are weak because of the orthogonality of the two "αβ" planes associated to these two harmonics. Thanks to (4) and for the considered seven-phase machine whose Φ_3/Φ_1=0.4 (and E_3/E_1=1.2), the torque under bi-harmonic current supply is 53% (resp. 26%) higher than this one obtained with only the first (resp. the third) harmonic current: the global torque is the sum of the torques produced in each "αβ" plane. With a same peak current, the bi-harmonic supply is obviously interesting.

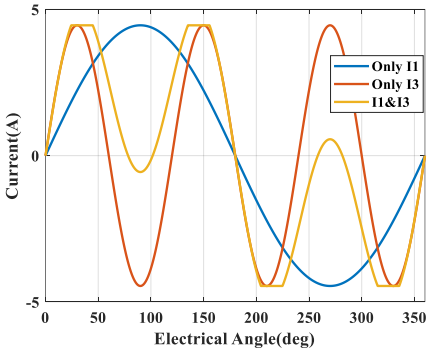

Fig. 13. Phase currents supply of the same peak value

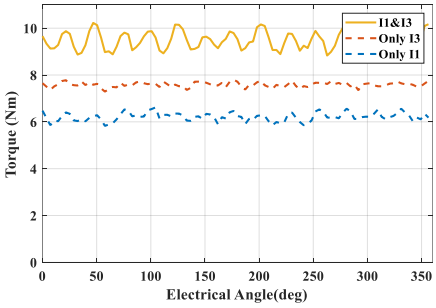

Fig. 14. Comparison of the torques under three kinds of supply at 600 rpm with

the same peak current for HFPM (6.2Nm/ 7.5Nm/ 9.5Nm)

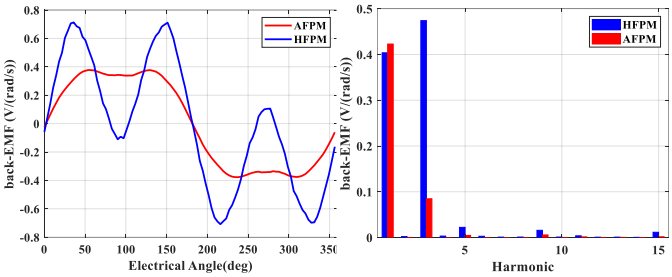

(a) (b)

Fig. 15. Comparison of back-EMF with (a) curves and (b) spectrum

D. Performance Comparison

The performance of the proposed HFPM machine is compared to the initial AFPM machine. Fig. 15 shows the comparison of back-EMF at no-load. It can be seen that the amplitudes of the 3rd harmonic back-EMF for the HFPM machine are significantly increased, 5 times higher than the one of AFPM. However, the fundamental component is slightly reduced 5%, due to the saturation of the SMC material with the addition of the 3rd radial rotor. Table IV shows the machine volume, mass, volume of magnet, torque density in volume, and the torque density in mass.

TABLE IV IMPACT OF ADDITION OF MAGNETS IN THE THIRD RADIAL ROTOR UNDER SAME PEAK CURRENT (4.45A IN FIG. 13)

Machine	Volume (dm^3)	Mass (kg)	Volume magnet (dm^3)	Torque (N.m)	Torque density (Nm/m^3)	Torque density (Nm/kg)
AFPM	1.693	9.21	0.03	6.3	3721	0.68
HFPM	1.693	9.01	0.10	9.5	5595	1.05
Variation (%)	0	-2	+233	+51	+50	+54

Under the same 4.45A peak current amplitude and bi-harmonic current supply, the output torque of the HFPM is increased by 51% compared to AFPM with two rotors, as shown in Fig. 16. (a). As consequence, the torque densities in volume and in mass are both significantly improved by 50% and 54%, as shown in Fig. 16. (b). The third rotor can be considered as an option to increase easily the torque with keeping the same volume of the machine.

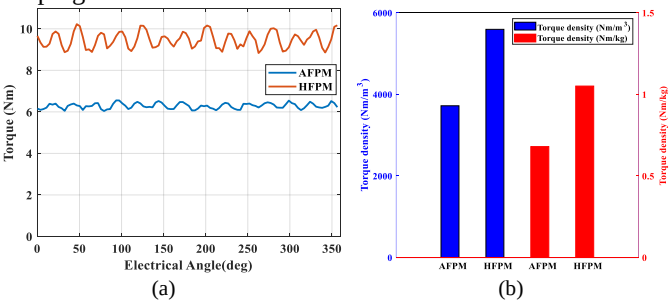

(a) (b)

Fig. 16. for a given RMS current, performance comparison with (a) torque and (b) torque densities of both SMC-stator and PM rotors AFPM and HFPM with MTPA strategy

The cogging torques of the both machines are shown in Fig. 17. The amplitudes of the cogging torque are similar and are both of small values, i.e. about 150mNm, and they are 2.3% of the rated output torque for the AFPM machine and 1.6% for the HFPM machine.

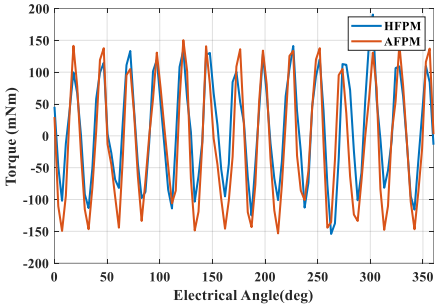

Fig. 17. The comparison of cogging torque

Using MTPA control strategy, the losses (copper and iron) and efficiency (without considering the mechanical loss) of the two machines are compared, i.e. AFPM and HFPM, as shown in Table V for a same RMS current and speed. The copper losses of AFPM is slightly higher than that of HFPM due to the different current supply strategy, i.e. the injection of 3rd harmonic current (limiting the peak current of HFPM, as shown in Fig. 13). Due to the addition of a third rotor and the injection of the 3rd harmonic current, the iron losses of HFPM is about three times of the AFPM. This is because the saturation of the stator is increased, due to the addition of the third rotor. The efficiencies of the both machines are similar, but with 51% more torque is obtained. If the same output torque is expected, 1.5 (9.5/6.3=1.5) times more current are needed according to Table IV, and the copper losses are increased to be 96W for the AFPM, then the efficiency is 80% instead of 86%. Moreover, the losses of VSI are also increased due to the increased current for transistors.

TABLE V THE COMPARISON OF LOSSES (COPPER AND IRON) FOR 3.15ARMS AT 600RPM

Machine	Copper loss (W)	Core loss (W)	Efficiency (-)
HFPM	40.23	65.41	85%
AFPM	42.59	21.92	86%

V. EXPERIMENTAL RESULTS

A. Prototype machine and test bench

Based on the previous analysis, a prototype of 7-phase, 28-slot, 12-pole/36-pole machine is designed and fabricated. Fig. 18 shows (a) the radial V-shaped rotor iron, (b) modular stator core and (c) the stator core with toroidal winding. Fig. 19 shows the test bench which includes the prototype machine, the load (a three-phase servo PM machine), a digital oscilloscope, power converter, control system based on DSP and FPGA, and DC power supply. The power converter consists in IGBT modules (PSS50S71F6) supplied from a DC power source. The prototype is controlled by a self-built control system (TMS320F28335, XC3S500E-PQ208, AD7606-6). The interface on the PC is developed in order to observe the signals, such as the speeds, the d-q currents and the torques, etc. The 7-phase prototype machine is mechanically connected to the torque sensor and loaded by the servo pm machine (constant torque mode).

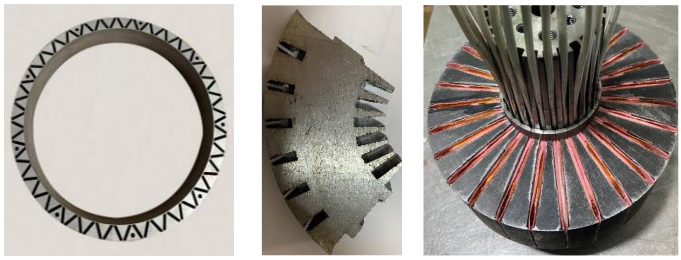

(a) (b) (c)

Fig. 18. Prototype of 7-phase machine. (a) V-shape radial rotor. (b) modular SMC stotor core. (c) stator with toroidal windings

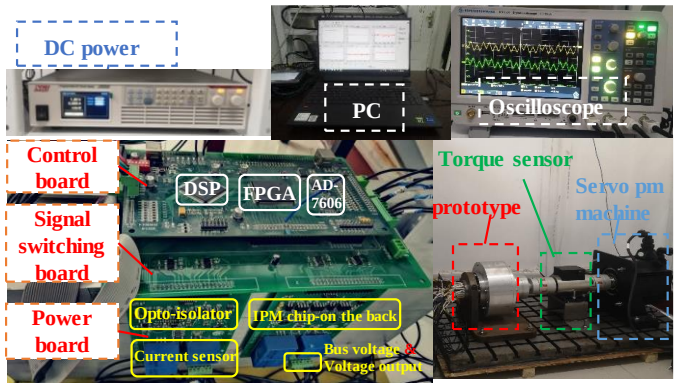

Fig. 19. The experimental test bench.

Based on the field-oriented control (FOC) theory, the control block diagram of the whole system is shown in Fig. 20. Using MTPA control strategy, the "Torque distribution" block generate the reference currents for multi-fictitious machines (M1, M3 and M5) as shown in the part II.C.1. The generated current waveform is similar to the back-emf waveform. The MTPA control strategy in detail for multiphase machine can be found in similar form in [30]. It can be found that we have in parallel three controls which are each similar to this one of 3-phase machine. The difference is that we have only one R(θ) rotation matrix for a 3-Phase for one dq frame. For a seven phase machine whose main harmonics are the first, the third and the fifth we have two other rotation matrix R(3θ) and R(5θ) which give two supplementary dq frames to be controlled with PI.

B. Back-EMF

In this test, the 7-phase machine is open-circuited and driven by a 3-phase servo pm machine at 100 rpm. The voltage between phase A and neutral point is recorded, and its related harmonic analysis is carried out. Fig. 21(a) presents the measured and FEM predicted back-emf divided by speed (V/rad/s) *Ke* over one electrical period. The harmonic content in Fig. 21(b) can be noted: the third harmonic is about 1.2 times the fundamental in numerical predictions and 1.71 for the experimental prototype. More precisely the difference is -18% for the third harmonic and -43% for the first harmonic. The differences may result from the manufacturing uncertainties, especially due to the complexity of the machine structure and additional mechanical structure in order to fix to the base. Moreover, the stator iron core is made by laser cutting which can decrease the magnetic saturation by more than 15% [34]. Nevertheless, it is possible to test the control by using different ratios of harmonics in the currents.

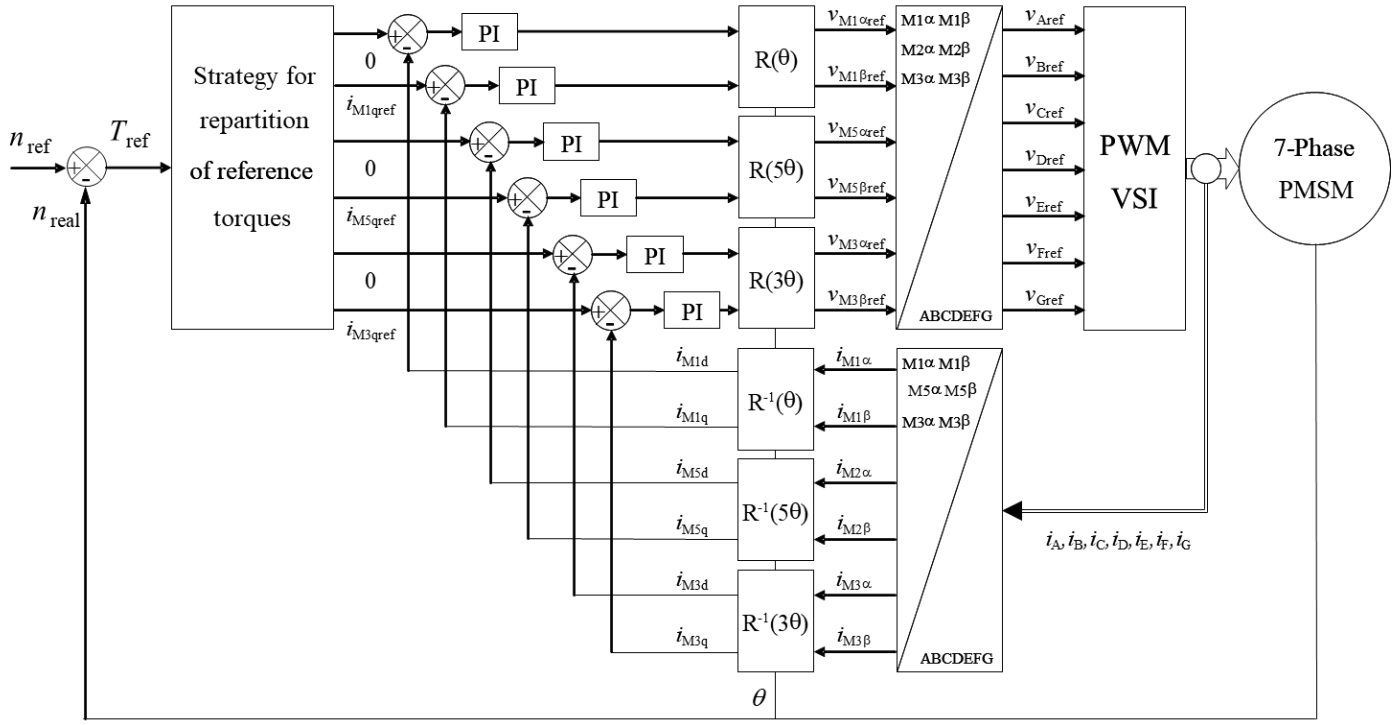

Fig. 20. FOC control block diagram

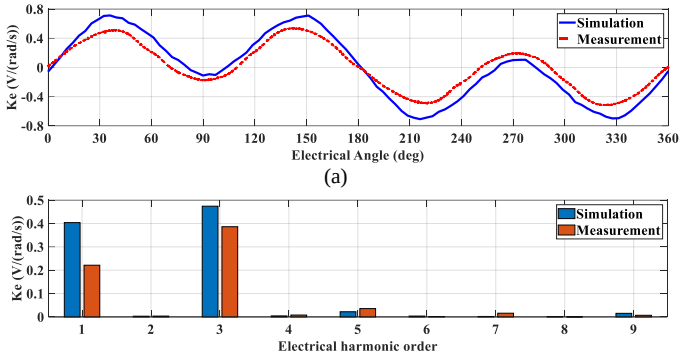

Fig. 21. (a) Measured back-emf for 1 rad/s and (b) its harmonic spectrum both for experimental and simulated HFPM

C. *Operation principle*

The specificity of the proposed machine is to develop torques of comparable values under three kinds of current supply: with only the first, the third or both the first and the third harmonics. Fig. 22 shows the injected current harmonics with the same load 1.5Nm at 100rpm. Among the three kinds of supply, the amplitude of only the first harmonic is more important than the other two strategies due to the small value of the back-emf. And the needed current of the other two strategies are with similar amplitudes.

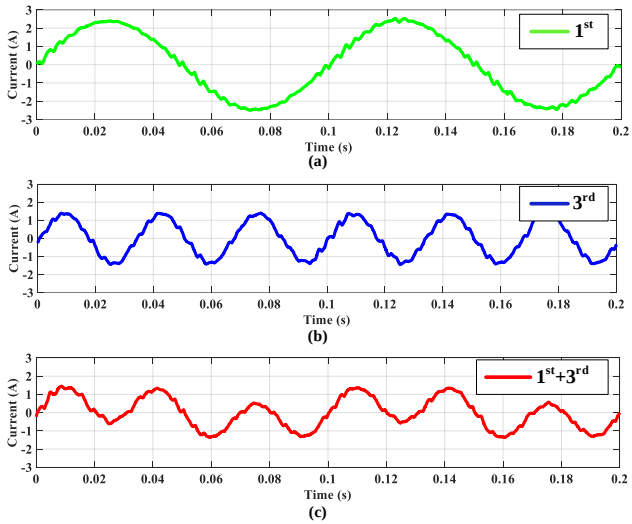

Fig. 22. Current supply with (a) only the first (b) only the third (c) both the first and the third harmonics with the same load 1.5Nm at 100rpm

In order to furtherly demonstrate the effectiveness of the proposed bi-harmonic machine, the torque-speed characteristic is evaluated. The control strategy whose objective is to find the maximum torque under voltage and current limits. The optimization problem to be solved is presented in (17).

$$x^* = \arg\min\left(-T_{em}(x)\right)$$

$$\text{with} \quad \max\left(U_1,...,U_7\right) \le 8\text{V} \qquad (17)$$

$$\max rms\left(I_1,...,I_7\right) \le 3.15\text{A}$$

$$x = \left[I_{1\max},\ \varphi_1,\ I_{3\max},\ \varphi_3\right]$$

Where T_{em} is the output electromagnetic torque, $U_1,\ldots,U_7$ are the amplitudes of voltage in phase, *rms* ($I_1,\ldots,I_7$) are the root mean square values of the current in phase, $I_{1,3\max}$ are the amplitude of the first and the third harmonic current, $\varphi_{1,3}$ are the phase angle of the first and the third harmonic current.

The obtained torque-speed characteristic curve is shown in Fig. 23. Experimental validations are performed and the results are marked by the circles. Two typical operation points are selected in order to illustrate the working principle, i.e. one point in the constant torque region and one in the constant power region. The needed current of the first operation point and its harmonic spectrum are also shown. The waveform is similar to the back-emf and I_3/I_1=1.8 compared to the measured E_3/E_1=1.71.

In the constant power region, only the third harmonic current is injected and the φ_3=0.4 rad which is not zero anymore compared to the one in the constant torque region.

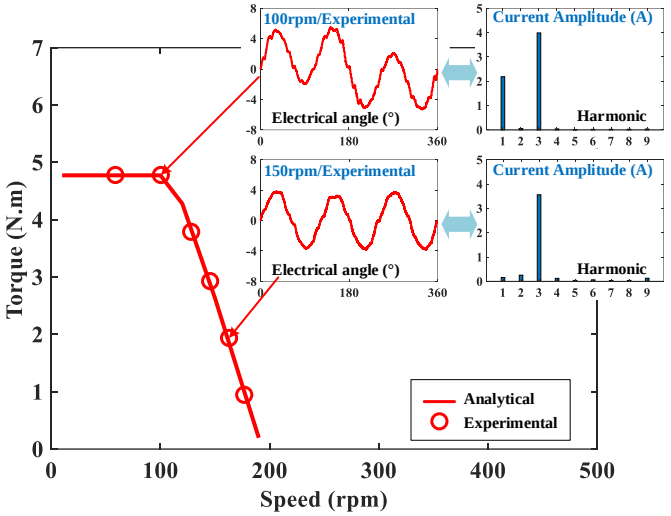

Fig. 23. Torque speed characteristics

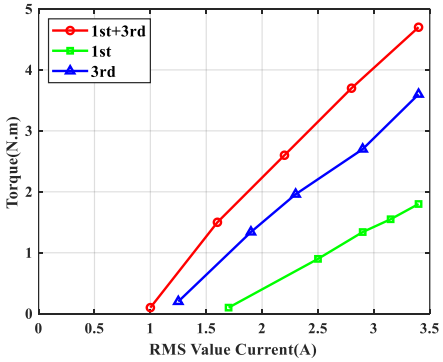

Fig. 24. Experimental mechanical Torques of the HFPM for different harmonic ratio of current at 100 rpm

TABLE VII THE COMPARISON OF TORQUE CURRENT RATIO

	P1 for H1	P3 for H3	P31 for H1+H3
Slope $7*E_k/\sqrt{2}$ from Fig. 21 (Nm/A)	0.225*7/1.414= 1.115	0.385*7/1.414= 1.9	0.446*7/1.414=2.2
Experimental slope from Fig. 24 (Nm/A)	1.23	2.04	2.47
Relative error	10%	7%	12%

D. *Torque-current ratio*

The mechanical torque performance is measured by torque sensor with respect to the variation of the current, as shown in Fig. 24. In order to validate the specificity of the bi-harmonic machine, the torques are measured with three kinds of current supply: with the fundamental only, third only or both the first and the third currents. With the same load, it can be noted that the required RMS value of current is the minimum with both the first and the third current supply, and the maximum with the fundamental current due to the small value of back-emf. With the predicted value obtained by measured of back-emf harmonic spectrum (Fig. 21), the slopes of Fig. 24 are compared and presented in Table VII. The relative error are less than 12%. The double polarity functionality of this machine can be considered as validated.

E. *The operation of the machine in different scenarios*

Fig. 25(a) shows the measured speed with MTPA control. The speeds with two conditions are tested, i.e. no-load and on-load. The reference speed is set to be 100rpm. The measured speed ripple of the both conditions are similar, i.e. ±0.5% of the reference speed. Therefore, the measured speed follows well with the reference one. Fig. 25 (b) shows the measured torque characteristics under no-load and on-load condition. The torque is measured by torque sensor and equal to 0.14Nm with no-load condition. The reference torque after the speed PI controller (shown in Fig. 20) is equal to about 1.85Nm in order to overcome the mechanical friction and the iron losses of the prototype. It can be seen that the torque ripples of the two conditions are always of small values.

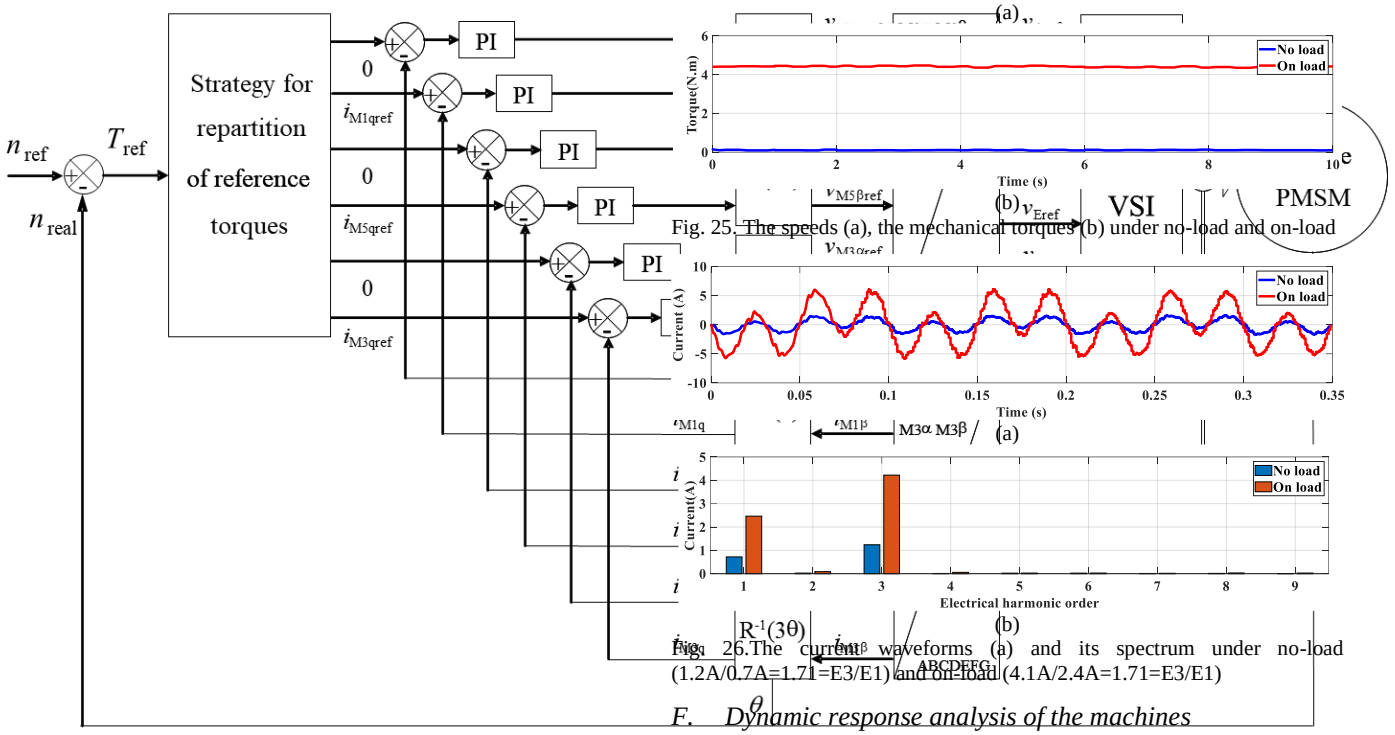

Fig. 25. The speeds (a), the mechanical torques (b) under no-load and on-load

The current waveforms and the harmonic spectrums of the both conditions are shown in Fig. 26. The ratio between the fundamental current and the 3rd harmonic current is 58%, which consists well with the ratio between the back-emf distribution E_1/E_3. Therefore, the ability of the machine to provide smooth torque with two harmonics of current, the fundamental and the 3rd, is confirmed.

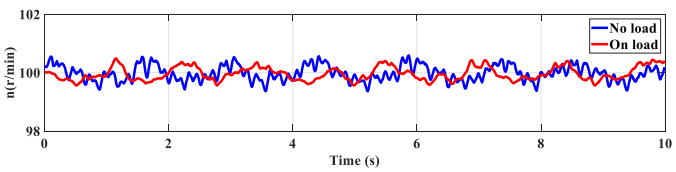

Fig. 26.The current waveforms (a) and its spectrum under no-load (1.2A/0.7A=1.71=E3/E1) and on-load (4.1A/2.4A=1.71=E3/E1)

F. *Dynamic response analysis of the machines*

The experimental dynamic response of the machine speed and torque, with the changing of the reference speed from 100rpm to 150rpm, are shown in Fig. 27(a) and Fig. 27 (b) respectively. It can be noted that the measured speed can follow the reference speed in 0.5 second with 10% overshoot.

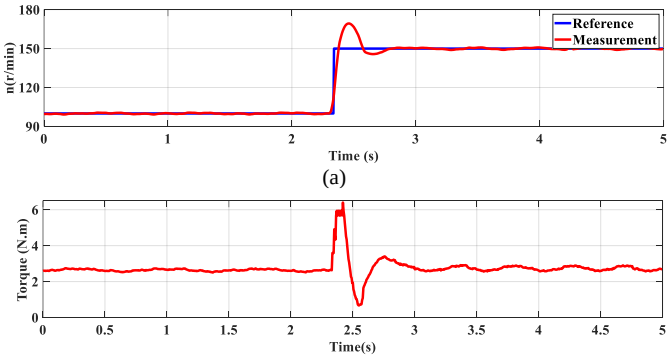

(b)

Fig. 27. The speeds (a) and the torque (b) response by changing speed

With the changing of load torque, the experimental dynamic response of the machine speed and torque are shown in Fig. 28. It can be noted in Fig. 28(a) that the measured speed can follow the reference speed in 0.3 second with also 10% variation.

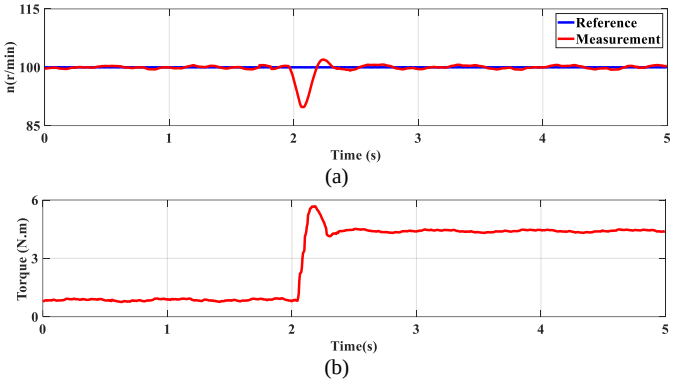

Fig. 28. The speeds (a) and the torque (b) response by changing load.

VI. CONCLUSION

This paper shows that a specific harmonic property of multi-phase machine can be used to increase the torque density by 50% of an initial 7-phase fault-tolerant AFPM. A radial third rotor with 3p pair poles has been added to an initial 7-phase AFPM with two external axial rotors with p pair poles. With the same global volume in the wheel and a same Voltage Source Inverter, higher performance are obtained but with an increase of the quantity of magnets. With 7-phase machine the torque quality is still guaranteed at low speeds by bi-harmonic vector control. This solution can be thus considered as a more expensive option for initial in-wheel motors with only two external axial rotors.

This fault-tolerant structure has also potential advantages for traction drive used for which flux-weakening and are necessary to obtain the constant power speed ratio required by the vehicle payload. By changing the polarity from 3p to p without modification of connection, the requirement for the flux –weakening ability is then reduced. The modification of the polarity is acting as an electromagnetic gearbox. Studies on this possibility will be investigated on the prototype in further works with adapted control algorithms.

REFERENCES

[1] S. Cai, J. L. K. Jr., and C. H. T. Lee, "Critical Review of Direct-Drive Electrical Machine Systems for Electric and Hybrid Electric Vehicles," *IEEE Transactions on Energy Conversion*. vol. 37, no. 4, pp. 2657-2668, Dec. 2022.

[2] C. J. Ifedi, B. C. Mecrow, S. T. M. Brockway, G. S. Boast, G. J. Atkinson, and D. K. Perovic, "Fault-tolerant In-wheel Motor Topologies for High-performance Electric Vehicles," *IEEE Transactions on Industry applications*, vol. 49, no. 3, pp. 1249-1257, May/June, 2013.

[3] A. Cavagnino, M. Lazzari, F. Profumo, and et al, " A Comparison Between the Axial Flux and the Radial Flux Structures for PM Synchronous Motors," *IEEE Transactions on Industry applications*, vol.38, no. 6, pp. 1517-1524, 2002.

[4] Y. B. Deshpande, H. A. Toliyat, and et al, "High-Torque- Density Single Tooth-Wound Bar Conductor Permanent-Magnet Motor for Electric Two Wheeler Application," *IEEE Transactions on Industry Applications*, vol. 51, no. 3, pp. 2123-2135, May/June 2015.

[5] Y. Yang, M. M. Rahman, T. Lambert and et al, "Development of an External Rotor V-Shape Permanent Magnet Machine for E-Bike Application," *IEEE Transactions on Energy Conversion*, vol. 33, no. 4, pp. 1650-1658, Dec. 2018.

[6] A. J. Rix, M. J. Kamper, "Radial-Flux Permanent-Magnet Hub Drives: A Comparison Based on Stator and Rotor Topologies, " *IEEE Transactions on Industrial Electronics*, vol. 59, no. 6, pp. 2475-2483, June 2012.

[7] M. A. Noroozi Dehdez and J. Milimonfared, "A Novel Radial–Axial Flux Switching Permanent Magnet Generator," in *IEEE Transactions on Industrial Electronics*, vol. 69, no. 12, pp. 12096-12106, Dec. 2022, doi: 10.1109/TIE.2021.3128901.

[8] W. Hua, H. Zhang, M. Cheng, J. Meng and C. Hou, " An Outer-rotor Flux-switching Permanent-magnet-machine with Wedge-shaped Magnets for In-wheel Light Traction" *IEEE Transactions on Industrial Electronics*, vol. 64, no. 1, pp. 69-80, Jan. 2017, doi: 10.1109/TIE.2016.2610940.

[9] W. Fei, P. C. K. Luk, J. X. Shen, Y. Wang, and M. Jin, "A Novel Permanent-Magnet Flux Switching Machine With an Outer-Rotor Configuration for In-Wheel Light Traction Applications," *IEEE Transactions on Industry Applications*, vol. 48, no. 5, pp. 1496-1506, Sep./Oct. 2012.

[10] D. Wu, Z. Xiang, X. Zhu, and et al, "Optimization Design of Power Factor for an In-Wheel Vernier PM Machine From the Perspective of Air-Gap Harmonic Modulation," *IEEE Transactions on Industrial Electronics*, vol. 68, no. 10, pp. 9265-9276, Oct. 2021.

[11] Y. Yu, F. Chai, Y. Pei, and M. Doppelbauer, "Investigation of PM loss in Spoke-Type Permanent Magnet Vernier Motors With Different Stator Topologies for In-Wheel Direct Drive, " *IEEE Transactions on Industry applications*, Vol. 58, no. 4, pp. 4562-4574, July/August 2022.

[12] S. P. Nikam, V. Rallabandi, and B. G. Fernandes, "A High-Torque-Density Permanent-Magnet Free Motor for in-Wheel Electric Vehicle Application," *IEEE Transactions on Industry Applications*, vol. 48, no. 6, pp. 2287-2295, Nov./Dec. 2012.

[13] J. Lin, N. Schofield, and A. Emadi, "External-Rotor 6−10 Switched Reluctance Motor for an Electric Bicycle," *IEEE Transactions on Transportation Electrification*, vol. 1, no. 4, pp. 348-356, Dec. 2015.

[14] H. Zhang, W. Hua, and Z. Wu, "Modular Spoke-Type Permanent-Magnet Machine for In-Wheel Traction Applications," *IEEE Transactions on Industrial Electronics*, vol. 65, no. 10, pp. 7648-7659, Oct. 2018.

[15] Y. Hua, C. Wang, Y. Liu, and et al, "Comparative Study of High Torque Density Spoke-Type PM In-Wheel Motors for Special Vehicle Traction Applications," *IEEE Transactions on Industry Applications*, vol. 58, no. 2, pp. 1952-1962, Mar./Apr. 2022.

[16] W. Geng, Z. Zhang, "Analysis and Implementation of New Ironless Stator Axial-Flux Permanent Magnet Machine With Concentrated Nonoverlapping Windings, " *IEEE Transactions on Energy Conversion*, vol. 33, no. 3, pp.1274-1284, September. 2018

[17] J. F. Gieras, R-J. Wang, M. J. Kamper, "Axial Flux Permanent Magnet Brushless Machines," *USA: Kluwer Academic Publishers*, 2004.

[18] A. Hemeida, M. Taha, A. A.-E. Abdalh, H. Vansompel, L. Dupré, P. Sergeant, "Applicability of Fractional Slot Axial Flux Permanent Magnet Synchronous Machines in Field Weakening Region," *IEEE Transactions on Energy Conversion*, vol. 32, no. 1, pp. 111-121, March 2017.

[19] Y. P. Yang, and D. S. Chuang, "Optimal Design and Control of a Wheel Motor for Electric Passenger Cars," *IEEE Transactions on Magnetics*, vol. 43, no. 1, pp.51-61, January. 2007.

[20] D. Winterborne, N. Stannard, L. Sjöberg, and G. Atkinson, "An Air-Cooled YASA Motor for in-Wheel Electric Vehicle Applications," *IEEE Transactions on Industry Applications*, vol. 56, no. 6, pp.6448-6455, Nov./Dec. 2020.

[21] L. Xu, Y. Xu, and J. Gong, "Analysis and Optimization of Cogging Torque in Yokeless and Segmented Armature Axial-Flux Permanent-Magnet Machine With Soft Magnetic Composite Core," *IEEE Transactions on Magnetics*, vol. 54, no. 11, pp.51-61, Nov. 2018.

[22] M. Polat, A. Yildiz, and R. Akinci, "Performance Analysis and Reduction of Torque Ripple of Axial Flux Permanent Magnet Synchronous Motor Manufactured for Electric Vehicles," *IEEE Transactions on Magnetics*, vol. 57, no. 7, pp.8106809, July 2021.

[23] N. Taran, V. Rallabandi, G. Heins, and D. M. Ionel, "Coreless and Conventional Axial Flux Permanent Magnet Motors for Solar Cars," *IEEE Transactions on Industry Applications*, vol. 54, no. 6, pp.5907-5917, Nov./Dec. 2018.

[24] C. Wang, J. Han, and et al, "Design and Optimization Analysis of Coreless Stator Axial-Flux Permanent Magnet In-Wheel Motor for Unmanned Ground Vehicle," I*EEE Transactions on Transportation Electrification*, vol. 8, no. 1, pp.1053-1062, March 2022.

[25] W. Geng, Y. Wang, J. Wang, J. Hou, J. Guo and Z. Zhang, "Comparative Study of Yokeless Stator Axial-Flux PM Machines Having Fractional Slot Concentrated and Integral Slot Distributed Windings for Electric Vehicle Traction Applications," *IEEE Transactions on Industrial Electronics*, vol. 70, no. 1, pp. 155-166, Jan. 2023. doi: 10.1109/TIE.2022.3151963.
[26] J. Gong, B. Zhao, Y. Huang, E. Semail, N. K. Nguyen, "Quantitative Comparisons of Outer-Rotor Permanent Magnet Machines of Different Structures/Phases for In-Wheel Electrical Vehicle Application," *Energies*, vol. 15, no. 18, pp. 6688, 2022.
[27] R. K. Dhawan, A. VA, "Multi-Phase Multi-Pole Electric Machine," *U.S. Patent* 20130257327A1, Oct. 3, 2013.
[28] F. Locment, E. Semail and F. Piriou, " Design and Study of a Multiphase Axial-flux Machine," *IEEE Transactions on Magnetics*, vol. 42, no. 4, pp. 1427-1430, April 2006, doi: 10.1109/TMAG.2006.872418.
[29] Aydin, S. Huang and T. A. Lipo, " Torque Quality and Comparison of Internal and External Rotor Axial Flux Surface-magnet Disc Machines," *IEEE Transactions on Industrial Electronics*, vol. 53, no. 3, pp. 822-830, June 2006, doi: 10.1109/TIE.2006.874268.
[30] F. Locment, E. Semail, X. Kestelyn, " Vectorial Approach-based Control of a Seven-phase Axial Flux Machine Designed for Fault Operation," *IEEE Transactions on Industrial Electronics*, vol. 55, no. 10, pp. 3682-3691, October 2008.
[31] J. Gong, H. Zahr, E. Semail, M. Trabelsi, B. Aslan, F. Scuiller, "Design Considerations of Five-Phase Machine with Double p/3p Polarity," *IEEE Transactions on Energy Conversion*, vol. 34, no. 1, pp. 12-24, March 2019.
[32] S. Huang, M. Aydin and T. A. Lipo, "TORUS Concept Machines: Pre-prototyping Design Assessment for Two Major Topologies," Conference Record of the 2001 IEEE Industry Applications Conference. 36th IAS Annual Meeting (Cat. No.01CH37248), Chicago, IL, USA, 2001, pp. 1619-1625 vol.3, doi: 10.1109/IAS.2001.955751.
[33] K. Wang, Z. Q. Zhu and G. Ombach, "Torque Improvement of Five-Phase Surface-Mounted Permanent Magnet Machine Using Third-Order Harmonic," *IEEE Transactions on Energy Conversion*, vol. 29, no. 3, pp. 735-747, 2014.
[34] F. Scuiller, F. Becker, H. Zahr, E. Semail, " Design of a Bi-harmonic 7-phase PM Machine with Tooth-concentrated Winding", *IEEE Transactions on Energy Conversion*, Vol 35, no. 3, pp 1567-1576, Sep. 2020.
[35] B. Aslan, E. Semail, J. Korecki, J. Legranger, "Slot/Pole Combinations Choice for Concentrated Multiphase Machines Dedicated to Mild-Hybrid Applications," in *Proc. 37th Annual Conference on IEEE Industrial Electronics Society (IECON)*, Vienna, Austria, Nov. 10-13, pp 3698 – 3703, 2013.
[36] F. Scuiller, E. Semail, and J. F. Charpentier, " General Modeling of the Windings for Multi-phase Ac Machines," *The European Physical Journal Applied Physics*, vol. 50, no. 03, pp. 1-15, 2010.
[37] P. B. Reddy, K. K. Huh, and A. M. EL-Refaie, "Generalized Approach of Stator Shifting in Interior Permanent-Magnet Machines Equipped With Fractional-Slot Concentrated Windings," *IEEE Transactions on Industrial Electronics.*, vol. 61, no. 9, pp. 5035-5046, Sep. 2014.
[38] P. Thelin, H. P. Nee, " Analytical Calculation of the Airgap Flux Density of PM Synchronous Motors with Buried Magnets Including Axial Leakage, Tooth and Yoke Saturations," *Eighth International Conference on Power Electronics and Variable Speed Drives*, London, UK, pp. 1-6, Sept. 2004.

VII. BIOGRAPHIES

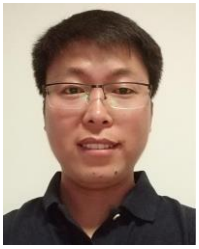

Jinlin Gong (M'13) received the B.Sc. degree from the Southwest Jiaotong University, Chengdu, China, in 2006. He got the M.S degree from Southwest Jiaotong University and the engineering degree from Ecole Centrale de Lyon in 2008, and received the Ph. D degree in electrical engineering from Ecole Centrale de Lille, France, in 2011. From October 2011 to August 2012, he was an Assistant Professor at the Engineering School of Arts et Métiers ParisTech, Lille, France. He is now an Associate Professor with the School of Electrical Engineering of Shandong University, Jinan, China. His research interests include optimal design and control of linear motors and multiphase synchronous motors.

XiuLin Wang graduated from Hunan University, China, in 2021. He is currently a master student in School of Electrical Engineering, Shandong University of China. His current research interests are multiphase motor drive control.

Benteng Zhao graduated from Shandong University of Science and Technology, Qingdao, China, in 2017. He got the M.S degree from Shandong University, Jinan, China, in 2020. Since Dec. 2020, he has been Research Assistant at China Astronaut Research and Training Center, Beijing, China. He specializes in motors and electrical appliances. His area of interest is design, modeling and simulation of multiphase machine.

Fei Tan received the B.S. degree from China University of Mining and Technology in 2019. She is currently a master student in School of Electrical Engineering, Shandong University of China. Her current research interests include optimal design of electrical machines.

Eric Semail (M'02) graduated from the Ecole Normale Supérieure, Paris, France, in 1986, and received the Ph.D. degree with a thesis entitled "Tools and studying method of polyphase electrical systems—Generalization of the space vector theory" from the University of Lille, France, in 2000. He became an Associate Professor at the Engineering School of Arts et Métiers ParisTech, Lille, France, in 2001 and a Full Professor in 2010. In the Laboratory of Electrical Engineering of Lille (L2EP), France, his fields of interest include design, modeling, and control of multiphase electrical drives

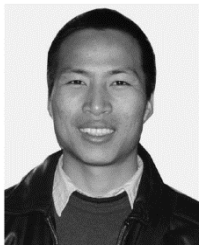

Ngac Ky Nguyen (M'13) received the B.Sc. degree in electrical engineering from the Ho Chi Minh City University of Technology, Vietnam, in 2005, and the Ph.D. degree in electrical and electronic engineering from the University of Haute Alsace, France, in 2010. Since September 2012, he has been an Associate Professor with the Laboratory of Electrical Engineering and Power Electronics of Lille, Arts et Métiers ParisTech, Lille, France. His research interests include modeling and control of

synchronous motors, power converters, and fault-tolerant multiphase drives. He has authored and co-authored more than 40 scientific papers and 5 book chapters.

Nicolas Bracikowski received the B.Sc. and M.Sc. degrees in electrical engineering from the University of Artois (France). He received his Ph.D. degree from Ecole Centrale de Lille (France), in 2012. Since 2013, he is an Associate Professor at Nantes University (France), where he carries out research in IREENA Laboratory (Institut de Recherche en Energie Electrique de Nantes Atlantique). His area research includes: optimal design of electrotechnical device, multi-physics lumped models and acoustic noise in electrical machine.